Vector Antenna and Maximum Likelihood Imaging for Radio Astronomy

Mary Knapp[1], Frank Robey[2], Ryan Volz[3], Frank Lind[3], Alan Fenn[2], Alex Morris[2], Mark Silver[2], Sarah Klein[2], Sara Seager[1]

[1]Massachusetts Institute of Technology
Department of Earth, Atmospheric, and Planetary Science
Cambridge, MA
mknapp@mit.edu
seager@mit.edu

[2]Massachusetts Institute of Technology
Lincoln Laboratory
Lexington, MA
robey@ll.mit.edu
ajf@ll.mit.edu
alexander.morris@ll.mit.edu
mark.silver@ll.mit.edu
sarah@ll.mit.edu

[3]Massachusetts Institute of Technology
Haystack Observatory
Westford, MA
rvolz@mit.edu
flind@haystack.mit.edu

***Abstract*[1]— Radio astronomy using frequencies less than ~100 MHz provides a window into non-thermal processes in objects ranging from planets to galaxies. Observations in this frequency range are also used to map the very early history of star and galaxy formation in the universe. Much effort in recent years has been devoted to highly capable low frequency ground-based interferometric arrays such as LOFAR, LWA, and MWA. Ground-based arrays, however, cannot observe astronomical sources below the ionospheric cut-off frequency of ~10 MHz, so the sky has not been mapped with high angular resolution below that frequency. The only space mission to observe the sky below the ionospheric cut-off was RAE-2, which achieved an angular resolution of ~60 degrees in 1973.**

This work presents alternative sensor and algorithm designs for mapping the sky both above and below the ionospheric cutoff. The use of a vector sensor, which measures the full electric and magnetic field vectors of incoming radiation, enables reasonable angular resolution (~5 degrees) from a compact sensor (~4 m) with a single phase center. A deployable version of the vector sensor has been developed to be compatible with the CubeSat form factor.

Results from simulation as well as ground testing of the vector sensor are presented. A variety of imaging algorithms, including expectation-maximization (EM), space-alternating generalized expectation-maximization (SAGE), projected gradient ascent maximum likelihood (PGAML), and non-negative least squares (NNLS), have been applied to the data. The results indicate that the vector sensor can map the astronomical sky even in the presence of strong interfering signals. A conceptual design for a spacecraft to map the sky at frequencies below the ionospheric cut-off is presented. Finally, the possibility of using multiple vector sensors to form an interferometer is discussed.

[1] This work was sponsored by the Assistant Secretary of Defense for Research & Engineering and the Department of the Air Force under Air Force Contract #FA8721-05-C-0002. Opinions, interpretations, conclusions and recommendations are those of the author and are not necessarily endorsed by the United States Government.
978-1-4673-7676-1/16/$31.00 ©2016 IEEE

TABLE OF CONTENTS

1. INTRODUCTION

The low frequency end of the electromagnetic spectrum (below 10 MHz) is one of the least explored windows in observational astronomy. Ground-based observatories including LOFAR [1], LWA [2], [3], MWA [4], and the proposed SKA-Low [5], [6] are improving access to the radio sky down to ~20 MHz, but these telescopes are fundamentally limited by the ionospheric cut-off frequency and experience significant ionospheric distortion even at higher frequencies due to scintillation, refraction, etc. The ionospheric cut-off frequency is the plasma frequency of the ionospheric peak, typically ~5-10 MHz depending on ionospheric conditions. Observations below this frequency are simply not possible from the surface of the Earth. In order to push to lower frequency observations, it is necessary to observe from space.

The low frequency end of the radio band offers insight into a wide range of non-thermal astrophysical processes as well as highly redshifted thermal processes [7]. Applications within the solar system include observations of solar coronal mass ejections (CMEs) and other solar radio bursts as well as planetary magnetospheres and their interaction with the solar wind and space weather. Beyond the solar system, low

frequency radio observations will enable mapping of the local interstellar medium (ISM) and perhaps the detection of exoplanetary magnetic fields in the solar neighborhood. Finally, low frequency observations that probe very high redshifts open a window into the cosmological Epoch of Reionization (EoR) and the birth of the first stars and galaxies. While some of these applications will require large interferometric arrays to obtain the necessary sensitivity, the critical first step is to map the low frequency sky at reasonable (~ few degree) resolution.

The only existing maps of the sky below 10 MHz come from the RAE-2 spacecraft in 1973 [8], [9]. This single spacecraft was placed in orbit around the Moon to avoid terrestrial noise, both natural and man-made. RAE-2 data were used to construct a partial map of the sky at several frequencies with a resolution of ~60 degrees [10]. There have been numerous proposals to design and build a multi-element interferometric array to map the sky at higher resolution (e.g. [11]–[13]), but none of these projects have yet been built and launched due to cost and complexity. Lowering the cost and complexity of such missions would help enable a wide range of new scientific investigations.

The advent of CubeSats has changed the landscape and increased the feasibility of a multi-spacecraft interferometric array. Such arrays have been proposed (e.g. [14]–[16]) and are a key step to lowering mission costs. It is still critical, however, to minimize the number of spacecraft required for such an array in order to keep costs and logistics reasonable. The vector sensor described in this work offers a more capable array element than the crossed dipoles typically used for ground-based low frequency interferometric arrays or the tripole antennas (dipole triads) often considered for space based arrays. When combined with appropriate signal processing, the extra degrees of freedom that the vector sensor provides will reduce the number of spacecraft needed for mapping the sky below 10 MHz both by increasing the sensitivity of each interferometric array element and by improving rejection of interfering sources. The potential for utilizing the vector sensor to provide characterization of strong interfering sources also opens the possibility of using these degrees of freedom to provide spatial pre-whitening. This offers the potential of making astronomically useful observations much closer to Earth than previously proposed missions, which often select Lunar orbits or surface installations to exploit the radio shadow of the Moon [7].

This paper is structured in three main parts. First, the vector sensor is introduced and described mathematically. A comparison of the vector sensor to a tripole antenna is presented as well. Second, several imaging algorithms for a single vector sensor are described along with imaging results for simulated vector sensor data. Third, two practical implementations of the vector sensor, one for ground-based testing and one for a CubeSat form factor, are presented.

2. VECTOR SENSOR

Determining the antenna to be used for low frequency mapping is an engineering tradeoff between complexity on a single spacecraft and system complexity in moving data between different nodes. Estimating the distribution of radio sources in space with a spatial aperture at the desired resolution of about 10 mrad, or 0.57 degrees, requires antennas distributed over a volume of space measured in hundreds of cubic kilometers[2]. Aperture synthesis requires the signals from each antenna be combined at a central node so the communication problem quickly grows as the number of receiving nodes increases. Measurement of source wave polarization state and the avoidance of antenna pattern nulls suggest that, at a minimum, each node should have a tripole antenna. We consider increasing the complexity of each node from the minimum tripole to reduce overall system complexity and cost.

The approach proposed is to use vector sensing, which is motivated by the following observations:

1. Vector sensors are able to determine direction of arrival of sources [17] without resorting to multiple poses as required for a triad.

2. Vector sensors maximize the statistics collected from a single point in space. This maximizes the utility of a single satellite short of deploying a spatial array and will provide a more capable interferometer with fewer spacecraft. While the final constellation is expected to contain multiple satellites, the ability to collect these statistics with a vector sensor allows radiometric imaging to be performed with a single spacecraft.

3. Vector sensors can null or isolate specific sources [18]. This potentially is of benefit in the near earth environment where background signal due to terrestrial sources can significantly reduce dynamic range.

The first of these has been published by other researchers (see [19]–[23]), but the second and third have not so we elaborate on them here.

Vector Sensor Description

An electromagnetic vector sensor (EMVS) samples the E and H field at a single location in space and with a common phase center. To do this, a vector sensor is

[2] The half-power beamwidth of an antenna is $\theta = \frac{\lambda}{D}$, where θ (in radians) is the 3 dB beamwidth in a particular direction, D is the projected aperture length in that dimension, and λ is signal wavelength. Resolution of 0.01 rad requires an antenna aperture larger than 100 wavelengths in each dimension. At 3 MHz where the wavelength is 100 m, the antenna length in each dimension must be 100m * 100 = 10km. The minimum volume to enclose this is $4/3\,\pi\,(10/2)^3 = 523$ km^3. Of course, aperture synthesis can reduce that volume for when the scene is stationary over the period of the measurement.

composed of three orthogonal dipole elements and three orthogonal loop elements. These six elements allow for a complete measurement of the E-field and B-field amplitude and phase of incoming radiation. The vector sensor is named for its capacity to fully measure the electromagnetic vector field rather than the single scalar measurement associated with a single element antenna. One consequence of sensing the full E and B vectors is that the vector sensor natively measures full polarization information.

Past work with vector sensors has been focused on determining the direction of arrival (DoA) and polarization for a small number of high SNR sources. We are concerned with imaging complex scenes with multiple low SNR sources, some of which may be spatially distributed.

Vector sensing of electromagnetic waves

Consider the electromagnetic field in space, characterized by the electric and magnetic fields in three spatial dimensions for a particular source, p,

$$\boldsymbol{\mathcal{F}}(p) = \begin{bmatrix} E_x(p) \\ E_y(p) \\ E_z(p) \\ H_x(p) \\ H_y(p) \\ H_z(p) \end{bmatrix}. \tag{1}$$

Free space is linear and the total field $\boldsymbol{\mathcal{F}_T}$ at any point is the superposition of sources,

$$\boldsymbol{\mathcal{F}_T} = \sum_{\boldsymbol{p=1}}^{\boldsymbol{P}} \boldsymbol{\mathcal{F}}(p). \tag{2}$$

Maxwell's Equations describe the relationship between the electric and magnetic fields and for free space Faraday's law, $\nabla \times \mathbf{E} = -\frac{\partial \mathbf{B}}{\partial t}$ and Ampère's law, $\nabla \times \mathbf{B} = \mu_0 \varepsilon_0 \frac{\partial \mathbf{E}}{\partial t}$ lead to the well-known definition of the Poynting, or source direction, vector $\mathbf{S} = \mathbf{E} \times \mathbf{H}$, and the relationship between the time-averaged intensity of the electric and magnetic field, $|\mathbf{H}| = \sqrt{\frac{\varepsilon_0}{\mu_0}}|\boldsymbol{E}|$. These equations then provide insight into the statistics that are possible with electromagnetic fields independent of the sensor used to make measurements of the fields. The first of these statistics, asserted without proof, is that the rank of the vector space $\boldsymbol{\mathcal{F}_T}$ is 6. For free space propagation and uncorrelated sources the spatial electromagnetic field covariance $\boldsymbol{C_{\mathcal{F}}}$ is the expectation,

$$\begin{aligned} \mathbf{C}_{\boldsymbol{\mathcal{F}}} &= \mathcal{E}(\boldsymbol{\mathcal{F}_T}\boldsymbol{\mathcal{F}_T^H}) \\ &= \mathcal{E}\left(\sum_{p=1}^{P} \boldsymbol{\mathcal{F}}(p) \sum_{p=1}^{P} \boldsymbol{\mathcal{F}}^H(p)\right) \\ &= \sum_{p=1}^{P} \alpha_p \, \mathbf{s}(p)\mathbf{s}^H(p), \end{aligned} \tag{3}$$

with $(\ )^{\boldsymbol{H}}$ denoting the Hermitian or conjugate transpose and with $\alpha_p \geq 0$ the source intensity for a source with electric and magnetic field relations noted by the signal vector $\mathbf{s}(p)$. In array signal processing, $\mathbf{s}(p)$ is normally referred to as the *steering vector*. $\mathbf{C}_{\mathcal{F}}$ is an N^2, or 36-element Hermitian symmetric covariance matrix that is a convex combination of the outer products of the source steering vectors. Since the terms above the upper diagonal completely define the terms below the diagonal, or vice versa, the maximum dimensionality of the linear vector space to which $\mathbf{C}_{\mathcal{F}}$ belongs is $\frac{N(N+1)}{2} = 21$. The terms along the diagonal of $\mathbf{s}(p)\mathbf{s}^H(p)$ are $|E_x(p)|^2, \left|E_y(p)\right|^2$, and $|E_z(p)|^2$ $|H_x(p)|^2, \left|H_y(p)\right|^2$, and $|H_z(p)|^2$. Any five of these define the sixth. This is a consequence of the relation, $|\mathbf{H}| = \sqrt{\frac{\varepsilon_0}{\mu_0}}|\mathbf{E}|$ (ε_0 and μ_0 are the permittivity and permeability of free space, respectively), or the square of both sides, $|\mathbf{H}|^2 = \frac{\varepsilon_0}{\mu_0}|\mathbf{E}|^2$, or in terms of the electric and magnetic field components, $|H_x|^2 + \left|H_y\right|^2 + |H_z|^2 = \frac{\varepsilon_0}{\mu_0}\left(|E_x|^2 + \left|E_y\right|^2 + |E_z|^2\right)$. This linear dependence reduces the dimensionality of $\mathbf{C}_{\mathcal{F}}$ from a maximum of 21 to 20.

Verification that this maximum dimensionality of the vector space defining the $\mathbf{C}_{\mathcal{F}}$ is the actual dimensionality has been verified by simulation. The results of the simulation are shown in Figure 1. In this simulation, field vectors, $\boldsymbol{\mathcal{F}}(p)$ for $P = 5000$ sources uniformly distributed in azimuth and elevation with random polarization angle and phase were created. The curves shown are the singular values of a data matrix created from a) the field vectors themselves, and b) from the Kronecker product of the field vectors, taking only the components that would be in the upper triangle of the field covariance matrix. The source SVD number where the singular value of the matrix is first zero (-infinity on the dB scale) indicates the dimensionality of the simulated matrix and thus the dimensionality of the electromagnetic field for free space propagation. Two additional curves are shown on this plot that will be discussed in the next section and indicate the dimensionality when sources are forced to lie in a plane and are of just a single polarization.

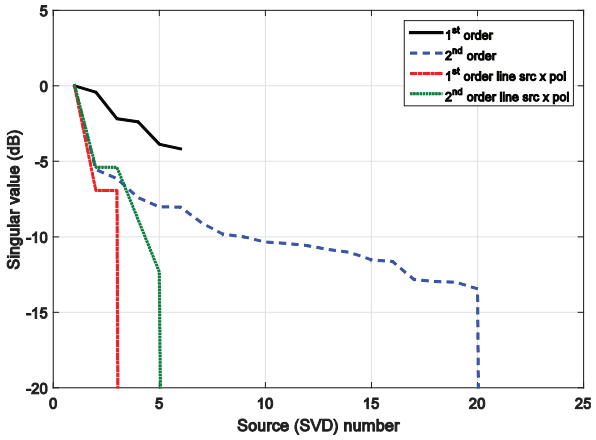

Figure 1. Simulation results illustrating the dimensionality of the first order (black) and second order (blue) statistics for free space propagation. A degenerate case where several sources with the same polarization are arranged in a line was also considered (red and green curves). The vector sensor can resolve n-1 sources, where n is the maximum SV shown above.

The dimensionality of this vector space is important because the dimensionality of a vector space determines the number of basis vectors required to span the space. Or, for this problem, that dimensionality determines the maximum number of sources that can be determined uniquely from a single point in space. The maximum number of sources that can be resolved from a single point in space using second order statistics is one less than the dimension, or 19 [24].

The maximum number of sources that can be determined from a single point (e.g. satellite) is a statistical property of electromagnetic fields and not of a specific antenna configuration. As much as possible, antenna designers attempt to sample the electromagnetic field. This sampling is in general a linear projection of the free space propagating waves onto the array manifold. A vector antenna samples all six elements of the electric and magnetic field. The linear projection operator is a diagonal 6-element matrix, which preserves the dimensionality of the covariance vector space.

Dropping any sensing element from the antenna reduces the dimensionality of the observed data. For an N (≤ 6)-element single-point in space antenna the dimension is $\frac{N(N+1)}{2}$. Dropping a single element of the vector sensor reduces the dimensionality to 15 and for a triad antenna the dimensionality is 6.

Situations that occur due to source and propagation configurations (e.g. in ground-based testing) can have a much lower limit on the number of sources that can be uniquely determined. The coordinate system for this problem is defined as follows. The x-y plane is parallel to the surface of the Earth, with +x pointing north and +z toward zenith. The spherical elevation coordinate, θ, is positive down from the z axis so θ=90° in the x-y plane. The azimuthal coordinate, ∅, is positive counterclockwise from the x axis. Electromagnetic waves traveling near the surface of the Earth are filtered such that only vertical polarization components remain. The vertically-polarized electromagnetic field vectors have the form,

$$\boldsymbol{\mathcal{F}}(p) = \begin{bmatrix} 0 \\ 0 \\ 1 \\ -\sin\emptyset \\ \cos\emptyset \\ 0 \end{bmatrix} E_z(p), \qquad (4)$$

where ∅, the azimuthal spherical coordinate, is determined by the direction to the particular source. The result of this degeneracy is that, in algebraic terms, vectors of this form only span a three dimensional proper subspace of the possible six and as a result, for first order statistics the maximum dimensionality of the vector space is 3. With a vector space dimensionality of 3 only two sources can be estimated unambiguously. Second order statistics can be analyzed as described earlier by examining $\boldsymbol{\mathcal{F}}(p)\boldsymbol{\mathcal{F}}(p)^{\boldsymbol{T}}$as these are the bases vectors for the covariance matrix**.** The non-zero terms of this product are a multiple of $[1, -\sin\emptyset, \cos\emptyset, -\sin\emptyset\cos\emptyset, \cos^2\emptyset, \sin^2\emptyset]$. Since $\sin^2\emptyset + \cos^2\emptyset = 1$ the dimensionality of the vector space spanned by $\boldsymbol{\mathcal{F}}(p)\boldsymbol{\mathcal{F}}(p)^{\boldsymbol{T}}$ is 5 so only four sources or less can be determined unambiguously from the second order statistics in this special case with sources in a plane and all of the same polarization. The red and green curves in Figure 1 are simulation results that illustrate these reduced dimensionality cases.

In free space the probability of three sources aligning in a plane with polarization vectors orthogonal to the plane would normally be considered a low or zero probability event. In ground based testing, however, this condition becomes a high probability event. Even in free space estimation of the intensity of the P sources when P is large is likely to lead to cases where the sources are nearly aligned. Multiple spacecraft, each with a vector antenna, can be used to resolve this degeneracy. The key observation is that the degenerate cases described are strictly a property of the electromagnetic field and are not related to the sensor orientation or design.

Internal sensor noise can increase the number of dimensions of the covariance vector space back to 21. The internal noise statistics are generally well calibrated and subtracting those statistics from the measurement statistics should result in a rank-deficient vector space for the spatial covariance matrix. Verification of this rank-deficiency provides a check that the noise statistics are well calibrated.

Vector sensor Signal-to-Interference plus Noise Ratio (SINR)

Here we compare the performance of a vector sensor with a tripole antenna/dipole triad as is commonly used aboard

spacecraft and show that there is at least a 3 dB improvement in sensitivity. The interfering source is assumed to be a strong manmade signal (e.g. radio station, radar) that is likely to be polarized and structured.

The optimal SINR when performing adaptive processing is

$$SINR = \alpha \mathbf{s}^H \mathbf{R}_\mathbf{n}^{-1} \mathbf{s}, \quad (5)$$

where $\mathbf{s}$ is the assumed (and actual) steering vector and $\mathbf{R_n}$ is the external and receiver noise covariance matrix. These equations directly apply to the vector or to a triad element and the improvement in SINR due to the use of a vector antenna over a dipole triad becomes apparent.

Consider a simplified background and receiver noise model

$$\mathbf{R}_n = \sigma \mathbf{I} + \beta \mathbf{d}\, \mathbf{d}^H \quad (6)$$

where the noise has a diagonal covariance matrix weighted by σ and there is a rank-1 interfering source with intensity β and characterized by a steering vector $\mathbf{d}$. Without loss of generality we can set $\mathbf{d}^H\mathbf{d} = 1$, and we can partition $\boldsymbol{d}$ into electric and magnetic components denoted d_E and d_H. With Maxwell's equations we can also scale $\mathbf{d}_E$ and $\mathbf{d}_H$ such that $\mathbf{d}_E^H\mathbf{d}_E = \mathbf{d}_H^H\mathbf{d}_H = 0.5$. The Sherman-Morrison-Woodbury formula applied to R_n is:

$$\mathbf{R}_n^{-1} = \frac{1}{\sigma}\mathbf{I} - \frac{\beta \mathbf{d}\mathbf{d}^H}{\sigma(\sigma+\beta)} \quad (7)$$

From equations (5) and (7), the optimal SINR for the vector antenna is expressed as

$$SINR_v = \frac{\alpha}{\sigma}\left(1 - \frac{\beta|\mathbf{s}^H\mathbf{d}|^2}{(\sigma+\beta)}\right). \quad (8)$$

We make use of the common definition relating the inner product in terms of the direction cosine, $|\mathbf{a}^H\mathbf{b}| = |\mathbf{a}||\mathbf{b}|\cos\gamma$ to simplify the expression and removing vector terms,

$$SINR_v = \frac{\alpha}{\sigma}\left(1 - \frac{\beta\cos^2\gamma}{(\sigma+\beta)}\right). \quad (9)$$

We can do the same for a triad,

$$SINR_T = \frac{\alpha}{2\sigma}\left(1 - \frac{\beta\cos^2\gamma_T}{(2\sigma+\beta)}\right) \quad (10)$$

where the subscript on γ_T indicates that the direction cosine is defined just with respect to the tripole elements of the steering vectors. The ratio of the optimal SINR indicates the potential gain of the vector antenna:

$$\eta = \frac{SINR_v}{SINR_T} = 2\frac{\left(1 - \frac{\beta\cos^2\gamma}{(\sigma+\beta)}\right)}{\left(1 - \frac{\beta\cos^2\gamma_T}{(2\sigma+\beta)}\right)}. \quad (11)$$

From this expression it is clear that for low noise, that is, $\beta = 0$ that a vector antenna will have a 3 dB advantage. For higher noise levels the advantage will be dependent on the direction cosine, which is a function of the polarization state and direction to the interference and desired signals. Figure 2 shows an example of the direction-dependent advantage of a vector sensor over a tripole for linear (top) and circular (bottom) polarization. The interfering source is located in the center of the map and is vertically polarized in both cases.

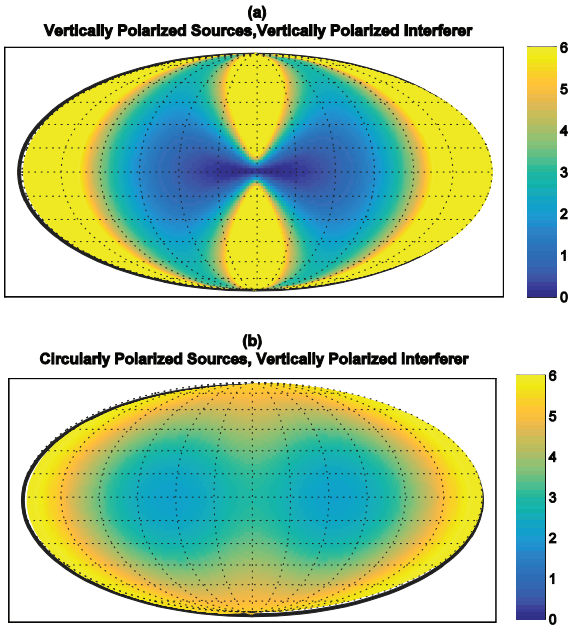

Figure 2. Comparison of the SINR (dB) provided by a vector antenna relative to that of a tripole antenna for a high interference-to-noise power ratio. The simulation is of a single interfering source and the relative SINR plotted shows the improvement provided as a function of the angle in space. The interfering source is at the center of the image and is vertically polarized. Plot (a) illustrates the gain for observing vertically polarized sources. Plot (b) shows the gain for right-circularly polarized sources. Referring to Equations 6-11, σ = 1, β = 100.

Signal Model

Our investigation concerns imaging far-field sources with propagation through a homogeneous but dispersive environment. We consider the case of uncorrelated sources since in problems of interest the time delay of any multipath is long relative to the inverse of the bandwidth and can thus be considered an independent source. The sensor may be undergoing motion and the sources are distant enough that only rotational motion need be modeled. Translational motion can be neglected.

The model used here for the EMVS data is that, K temporal samples, indexed by k are taken from the N vector sensor elements. The source field is also discretized into I pixels (alternative models are discussed in Section 6). For problems of interest the propagation medium can be

polarizing and the EMVS is polarization sensitive. Two polarization bases are used, either right and left circular or horizontal and vertical linear, to span the polarization space. We use a single index, $i = 1, \ldots, I$ into the entire three-dimensional array. As a result, there will be I cells with discretization over both spatial angles and polarization state. In each source cell radiation is assumed to be created from a complex white Gaussian process. The received data vector, $\mathbf{z}[k]$, is

$$\mathbf{z}[k] = \sum_{i=1}^{I} c_i[k]\mathbf{a}_i + \mathbf{n}[k], \tag{12}$$

where the receiver noise, $\mathbf{n}[k]$, is a white complex zero-mean Gaussian process, $CN(0, \mathbf{R}_n)$. The $\mathbf{a}_i$ are the steering vectors corresponding to the i^{th}cell and the $c_i[k]$ are the temporal samples of the source noise process, assumed to be generated by a process that is $CN(0, \sigma_i)$.. Equation (12) can be expressed in matrix-vector notation as

$$\mathbf{Z} = \mathbf{AC} + \mathbf{N}. \tag{13}$$

In this equation, $\mathbf{Z}$ is a matrix whose columns are the $\mathbf{z}$[k], $\mathbf{A}$ is a matrix whose columns are the $\mathbf{a}_i$, the columns of $\mathbf{C}$ are vectors of $c_i[k]$, and the columns of $\mathbf{N}$ are the vector noise samples, $\mathbf{n}[k]$.

The following is the log-likelihood for this data set;

$$l = KN\ \log\pi - K\log\|\mathbf{R}\| - \ K\,\mathrm{tr}\,\mathbf{R^{-1}S}, \tag{14}$$

and in this equation, the sample covariance matrix is

$$\mathbf{S} = \frac{1}{K}\,\mathbf{Z}\,\mathbf{Z}^{\mathrm{H}}, \tag{15}$$

3. IMAGING ALGORITHMS

Using simulated vector sensor data, a linear beamforming approach and a variety of nonlinear iterative algorithms have been developed and tested. The linear imaging was shown to be wholly inadequate as expected, and testing of the nonlinear algorithms is ongoing. These algorithms fall into two broad categories that optimize different objectives: maximum likelihood and least squares with respect to measurement covariance. Maximum likelihood approaches include expectation-maximization (EM) [25], [26], [32]-[38]. space-alternating generalized expectation maximization (SAGE) [27], proximal gradient ascent [28], and regularized versions of those. The least squares approaches include both basic least squares and L_1-regularized least squares, and both are based on the proximal gradient algorithm. Including regularized and hybrid methods, 13+ distinct algorithm variants were developed and tested. This work describes linear imaging, EM, and projected gradient ascent in detail. An in-depth comparison of the performance of all algorithms and variants will be the subject of a future publication. Note that the formalism below works for estimating polarization of sources as well as location, but for simplicity in this work we concentrate primarily on estimating direction of arrival.

Linear Imaging

The baseline algorithm for spectral estimation is linear projection.

$$\mathbf{I_L} = \mathbf{AZ} \tag{16}$$

In the examples described later in this paper, the $\mathbf{A}$ are separated into a Stokes bases. These bases allow the cell with the maximum absolute amplitude to be selected and further examined for polarization characteristics again using linear projection.

This imaging algorithm does not take advantage of knowledge of the receiver covariance matrix and each cell is estimated independently with no interaction to improve the results. As will be seen, the ability to resolve multiple sources with a single vector antenna using linear imaging is poor. Creating an image with multiple sources requires the use of higher order statistics. Eventually, an array of vector sensors employing array synthesis, where the pose and location of each element changes over time to fill in the UV, or direction cosine, space will be used to produce more complex images that well represent the true sky.

Expectation Maximization

Expectation-maximization (EM) algorithms for similar data models has been derived in several other publications ([24], [29], [32]-[38]) therefore the formalism of generating the algorithm will not be repeated here. The steps of the algorithm are as follows:

1. Initialize the complete data spectral estimates $\mathbf{\Sigma^1}$ and covariance matrix, $\widehat{\mathbf{R}}^1 = \mathbf{A}\widehat{\mathbf{\Sigma}}^1\mathbf{A}^H + \mathbf{R_n}$.
2. Iterate the following for $p = 1 \ldots P$:

$$\widehat{\mathbf{\Sigma}}^{p+1} = \mathrm{diag}\left(\widehat{\mathbf{\Sigma}}^p + \widehat{\mathbf{\Sigma}}^p\mathbf{A}^H\left(\widehat{\mathbf{R}}^{p^{-1}}\mathbf{S}\widehat{\mathbf{R}}^{p^{-1}} - \widehat{\mathbf{R}}^{p^{-1}}\right)\mathbf{A}\widehat{\mathbf{\Sigma}}^{\mathbf{p}}\right) \tag{17}$$

$$\widehat{\mathbf{R}}^{p+1} = \mathbf{A}\widehat{\mathbf{\Sigma}}^{p+1}\mathbf{A}^H + \mathbf{R_n} \tag{18}$$

As noted ([24], [29], [32]-[38]), these iterations take the form of a gradient ascent algorithm since the diagonal terms of

$$\mathbf{A}^H\left(\widehat{\mathbf{R}}^{p^{-1}}\mathbf{S}\widehat{\mathbf{R}}^{p^{-1}} - \widehat{\mathbf{R}}^{p^{-1}}\right)\mathbf{A} \tag{19}$$

are the gradients of the log-likelihood with respect to each of the elements of $\mathbf{\Sigma}$, and stationary points are where either this gradient is zero for elements of $\mathbf{\Sigma}$ that are non-zero or will be negative or zero for elements of $\mathbf{\Sigma}$ that are zero. This formulation then leads directly into the projected gradient ascent algorithm.

Projected Gradient Ascent

The primary problem with a basic gradient ascent algorithm is that it readily produces infeasible solutions by allowing indefinite values of $\mathbf{\Sigma}$. EM avoids this problem by pre- and post-multiplying the gradient term by $\mathbf{\Sigma}$. Another approach is to employ a form of projected gradient ascent, in which negative eigenvalues of $\mathbf{\Sigma}$ are set to zero after every gradient step, guaranteeing a non-negative definite solution. Note that, as with EM, such a solution is not guaranteed to achieve the global maximum since the log-likelihood function is not concave [30]. Since projected gradient ascent is a form of the proximal gradient algorithm for which there are numerous enhancements, we employ an accelerated version with variable step size from [31] and adaptive restart from [32]. Excluding these additions, the basic projected gradient algorithm for diagonal $\mathbf{\Sigma}$ takes the following form:

1. Initialize the step size μ, spectral estimates $\mathbf{\Sigma}^1$, and covariance matrix

$$\widehat{\mathbf{R}}^1 = \mathbf{A}\,\widehat{\mathbf{\Sigma}}^1\mathbf{A}^H + \mathbf{R_n} \tag{20}$$

2. Iterate the following for $p = 1 \ldots P$:

$$\nabla = \mathrm{diag}\left(\mathbf{A}^H\left(\widehat{\mathbf{R}}^{p^{-1}}\mathbf{S}\widehat{\mathbf{R}}^{p^{-1}} - \widehat{\mathbf{R}}^{p^{-1}}\right)\mathbf{A}\right) \tag{21}$$

$$\widehat{\mathbf{\Sigma}}^{p+1} = \max\left(0,\, \widehat{\mathbf{\Sigma}}^p + \mu\,\nabla\right) \tag{22}$$

$$\widehat{\mathbf{R}}^{p+1} = \mathbf{A}\,\widehat{\mathbf{\Sigma}}^{p+1}\mathbf{A}^H + \mathbf{R_n} \tag{23}$$

Higher Order Spectral Estimation

The algorithms described thus far have used as inputs the second order statistic in the form of the sample covariance matrix in estimation of the spatial spectrum. These algorithms were found to converge but not necessarily to the truth when the number of sources was greater than five, which is the number of elements in a single vector sensor minus one. With more sources than five initializing the estimated spatial spectrum in simulation with the truth yielded a stable point in the iterative algorithms. This presence of local maxima in the likelihood suggested several alternatives to ensure convergence.

The first approach is to increase the number of vector sensors where the spatial separation between vector sensor phase centers will resolve the ambiguity by changing the shape of the likelihood surface. This is the approach that we expect to use when actually collecting radio astronomy data, but for the purpose of this paper we investigated an alternative, namely using higher order statistics to improve convergence. The higher order statistics approach is suggested based on the results of the Section "*Vector sensing of electromagnetic waves*." In this algorithm the iterations are as described in Equations (17) and (18) but use the second order statistics as inputs and estimate the spectrum and the covariance matrix using fourth order moments. That is, we use as input data the matrix $\tilde{\mathbf{Z}}$ whose columns are formed from the first order array samples as the unique elements of $\mathrm{vec}(\mathbf{z}[k]\mathbf{z}^{\mathrm{H}}[k])$. Using these length-20 vectors increases the size of the covariance matrix R to a 20 by 20 matrix but as shown in the next section has benefits for convergence in some cases.

4. Simulation Results

Spatial sampling, simulated source generation, and algorithm initialization

Simulated sky maps and test patterns were generated using equal area sampling of a sphere rather than a regular grid in spherical coordinates. A grid with equal spacing in elevation and azimuth oversamples the poles and undersamples the equatorial region, leading to poor convergence and distortions in the resulting images. A MATLAB implementation of the HEALPix [33] library developed by JPL was used to generate a list of sample points that are equally spaced over 4π steradians. Fairly coarse sampling was used for the simulations presented here (3072 pixels over the sphere, each pixel is approximately 13 square degrees) in the interest of reasonable simulation runtimes. Tests with higher resolution indicated that there was little loss of fidelity due to the decreased simulation resolution.

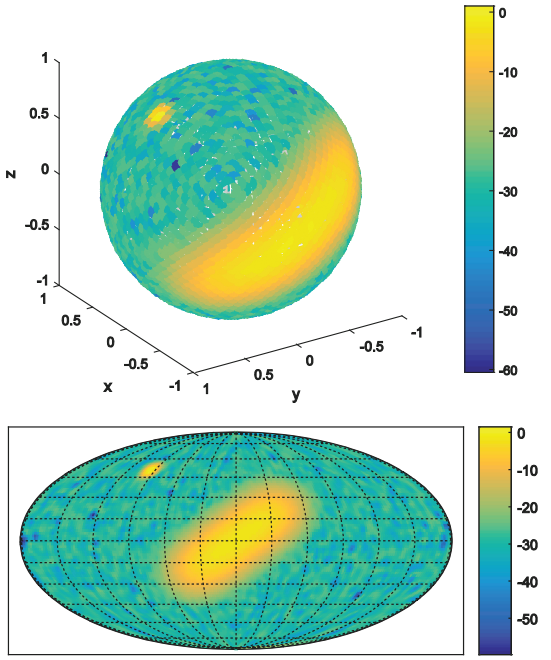

Figure 3. Simple simulated sky maps. The sampling of the sky map was generated using HEALPix. The simulated point and distributed sources shown were used to generate simulated input for algorithm testing. The pixel values are normalized and the colorscale represents intensity in dB. The top view shows the model sky on a sphere. Individual pixels are visible. The bottom view is a smoothed Mollweide projection of the same simulated sky.

As illustrated in Figure 3, discrete sources, representing unresolved bright radio sources, were modeled either as single bright pixels or as low variance bivariate Gaussian distributions. Spatially distributed sources (e.g. the galactic plane or other bright resolved object) were modeled as Kent (FB_5) [34] distributions. A Kent distribution is a bivariate Gaussian distribution recast onto the surface of the unit sphere. A small Gaussian noise component was added to each pixel of the simulated sky map. All pixel values in the map were constrained to be positive.

Results: Discrete sources

The dimensionality argument from Section 2 indicates that the vector sensor should be able to resolve up to 19 sources if higher order statistics are exploited correctly. In order to test this assertion, point sources of varying intensity were scattered randomly across a sphere. This model 'sky' was sampled many times to produce a time series input to the EM algorithm. When the point sources were modeled as white Gaussian processes across the full time range of the simulation, up to 5 sources could be resolved when a uniform distribution of energy was used to initialize the estimation algorithms (Figure 4). This limit on resolution was almost certainly due to local maxima in the log-likelihood since initializing the algorithms with a solution that was close to the truth and with more sources than 5 would converge. When the sources were instead impulsive, meaning each source appears only once in the time series, up to 18 sources could be resolved (Figure 5) even with the uniform distribution for initializing the estimators. This approaches the theoretical number of sources that we expect to resolve when fully exploiting higher order statistics.

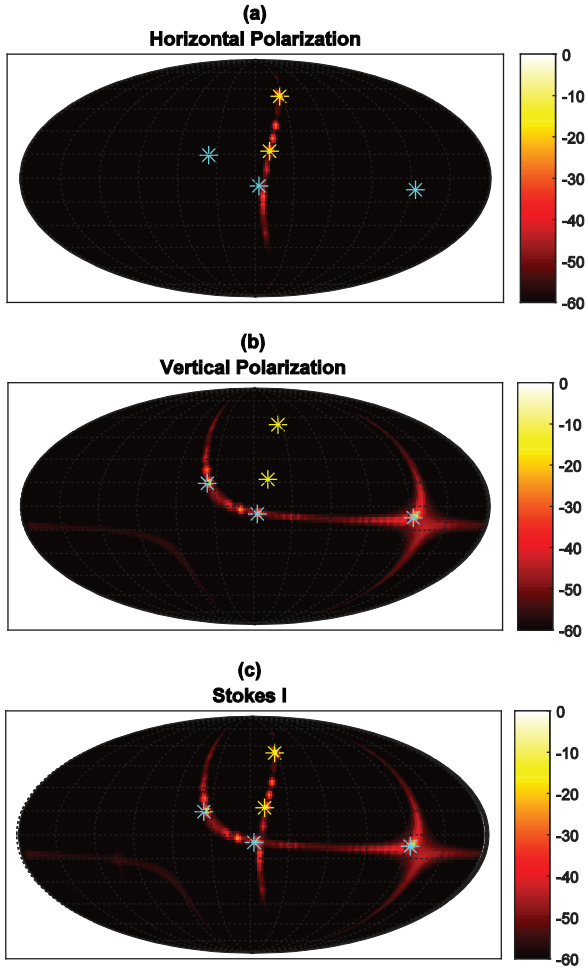

Figure 4. Results from simulation with 5 white Gaussian sources. The top map (a) shows horizontally polarized sources only while the middle map (b) shows vertically polarized sources. The bottom map (c) shows total intensity (both polarizations). The yellow (horizontal polarization) and cyan (vertical polarization) '*' markers denote the true position of each source. The EM algorithm was able to detect all of the sources correctly. The colorscale represents dB. The curving lines are algorithm artifacts or sidelobes and are 40-50 dB below the peak levels.

While the current algorithm performance for true Gaussian sources is below what is theoretically possible, the vector sensor is still able to detect the direction and polarization of multiple sources from a single pose. Algorithmic

development is ongoing to improve performance for truly Gaussian sources. The ease with which the algorithm detects impulsive, non-Gaussian sources maybe of use for detecting and nulling interfering terrestrial signals.

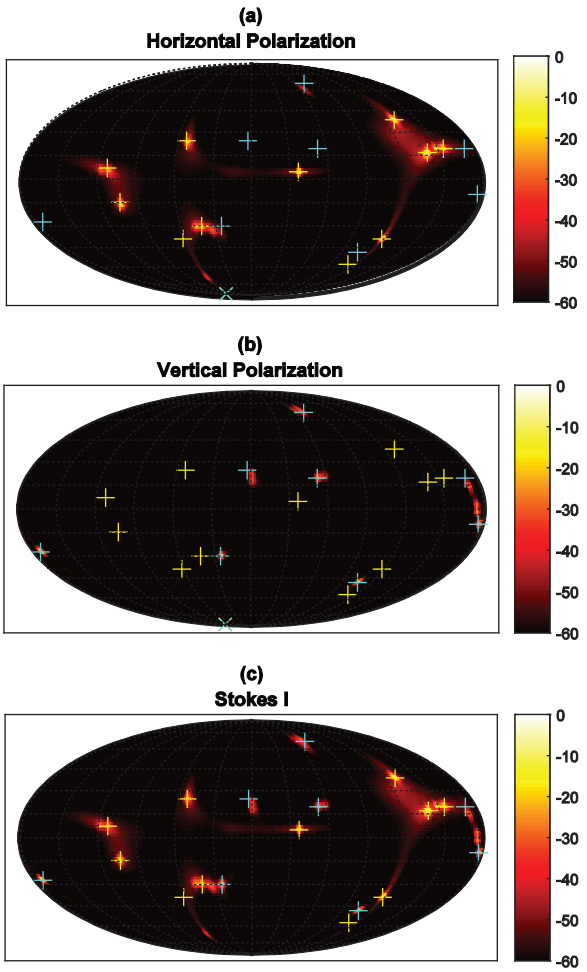

Figure 5. Results from simulation with 19 impulsive point sources. The top map (a) shows horizontally polarized sources only while the middle map (b) shows vertically polarized sources. The bottom map (c) shows total intensity (both polarizations). The yellow (horizontal polarization) and cyan (vertical polarization) '+' markers denote the true position of each source. The EM algorithm was able to detect all but one of the sources correctly. The color scale represents dB.

Results: Spatially distributed sources

Imaging distributed sources is a key step towards using the vector sensor for astronomical imaging. At low radio frequencies, the galaxy appears as a distributed source that stretches across most of the sky. Figure 6 below show the results of the EM algorithm for a simple sky model containing a large distributed source and a point source (Figure 3).

The EM algorithm is somewhat biased toward finding peaks, so various smoothing penalties are being investigated to improve imaging of spatially distributed sources. While such additions to the basic EM algorithm may improve detection of distributed sources, ultimately a different approach may be required to accurately capture distributed sources. Using a different sky model, such as a spherical harmonic decomposition, would lend itself to distributed sources more readily than point sources. Adding more vector sensors to form an interferometer would increase the number of available degrees of freedom, therefore making it easier to resolve distributed sources within the traditional pixel model framework.

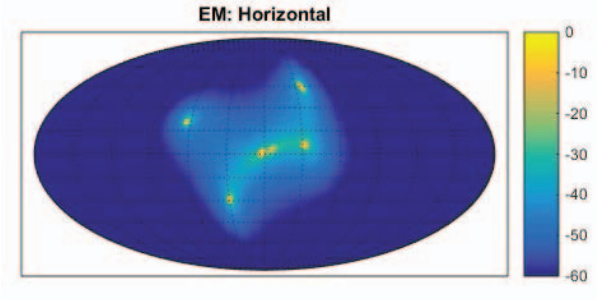

Figure 6. Initial EM algorithm result for simple sky model (Figure 3). This result was generated from a single time 'snapshot' of the sky model. The image is normalized and the colorscale represents dB. The EM algorithm is somewhat biased toward finding peaks, so various smoothing penalties are being investigated to improve imaging of spatially distributed sources.

5. Field Testing

An Electromagnetic Vector Sensor (EMVS) Implementation

An electromagnetic vector sensor for use in the HF band (3-40 MHz) has been implemented. The current sensor is designed for ground-based use and two copies (designated Atom 1 and Atom 2) have been created to enable basic interferometric experiments. The vector sensor design used for ground-based testing is composed of three orthogonal rings approximately 1 m in diameter (Figure 7). Each of the rings has two ports that are connected to a sum and difference hybrid. The result is that each physical loop serves as both a dipole and a loop. The full antenna produces the six output channels consistent with measuring each component of the electromagnetic field, referenced to the orientation planes of the three loops. A design appropriate for space based application on a CubeSat platform is also under development. A different mechanical design (but similar electrical design) is needed in order to stow the antenna for deployment from a spacecraft. The deployable design is described in Section 7.

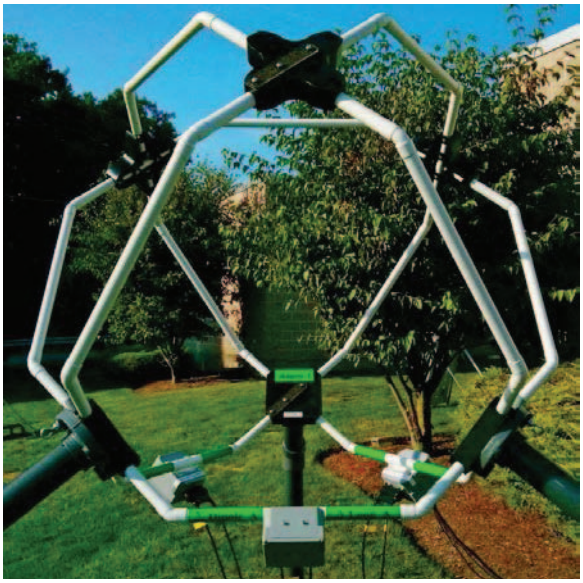

Figure 7. Atom 1 vector antenna at MIT Haystack Observatory. The three octagonal loops that form the vector sensor are painted copper tubing and the support posts are PVC. Each loop is 40" in diameter. This vector sensor is intended for ground testing only.

Test Plan Description

Initial testing of the Atom 1 and 2 vector sensors is currently being conducted at MIT Haystack Observatory in Westford, MA. A more extended observational campaign is currently planned at Owens Valley Radio Observatory (OVRO). The OVRO site, near Bishop, CA., was chosen for two primary reasons: it is radio quiet and it is also the location of the Owens Valley LWA [3] site, which will provide an independent, simultaneous measurement of the same sky under the same conditions. Sky maps produced by the OV LWA using traditional interferometric techniques will be compared to maps produced by the covariance-based mapping approach used with vector sensor data in order to assess the vector sensor's mapping capability.

The data collected during the OVRO testing will be used to assess the sensor and algorithm capabilities of a single vector sensor as well as multiple vector sensors with ~1 km baselines between them.

Finally, the algorithms described in this work will be applied to short snapshots of raw LWA data to validate their applicability to interferometric arrays with many elements.

Initial Results

Initial testing of the Atom 1 and Atom 2 vector antennas is in progress at MIT Haystack Observatory in Westford, MA. An initial test was the detection and mapping of the NIST WWV 15 MHz transmission [35]. Figure 8 shows spectrograms from each element of Atom 2 (top) and a map produced from the same data (bottom). An improved LNA design for the Atom antennas is underway. Noise characterization for the full system is also underway in advance of the planned field testing campaign. The results presented here are preliminary, but do indicate that the vector sensor is functioning properly and is able to localize bright sources.

MIT Haystack Observatory is relatively close to Boston, MA., so the strongest ambient signals are man-made. Scheduled testing at the radio quiet Owens Valley site should allow for improved sky imaging at frequencies above the ionospheric cut-off.

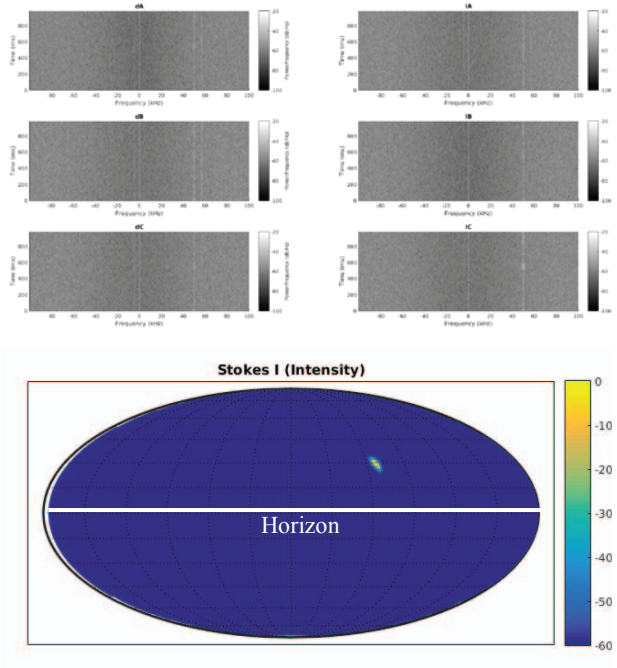

Figure 8. Spectrograms from each Atom element (top) and source image generated using projected gradient ascent (bottom). The left column spectrograms are from the dipole elements and the right column spectrograms are from the loops. Frequency is on the x-axes and time increases upward on the y-axes of the spectrograms. This measurement is 200 kHz wide and centered at 14.95 MHz. The WWV signal is clearly visible at 15 MHz (+50 on the horizontal scale) in the spectrograms and also appears in the map below. The signal at 0 in the spectrograms is an FFT artifact. The source map coordinates are local elevation and azimuth, with 0 azimuth (local horizon) marked by the white line.

Calibration

Well known radio sources (e.g. Cas A, Cyg A, Vir A) will be used to calibrate the flux received in ground testing. Directional antenna element pattern verification has been accomplished by rotating the antenna in the presence of a strong reference signal. More accurate calibration and verification of element patterns will be undertaken on the final antenna and receiver design prior to launch.

6. APPLICATION TO INTERFEROMETRY

Vector sensor elements can naturally be used in arrays to perform interferometric observations. The increased degrees of freedom available from the vector sensor element will increase the capability of an array to determine the properties of independent sources or to produce brightness distribution images from UV plane measurements in combination with an appropriate image deconvolution approach. Initial work in this area includes that of Han & Nehorai 2014 [22] which discusses vector sensor arrays in the context of linear nested arrays, the co-array formalism, and a tensor modelling approach. Additional work is needed to extend interferometric vector sensor processing to arbitrary two and three dimensional configurations.

The algorithm development described in this work is focused on mapping the astronomical sky with a single 6-element vector sensor. The larger goal, however, is to demonstrate that an interferometric array composed of vector sensors will be more capable than an array composed of an equal number of scalar sensor elements. Additionally, the imaging approach described in previous sections uses a 'pixel' model of the sky where the imaging algorithm attempts to estimate the flux and polarization from each pixel under the assumption that each pixel represents a Gaussian random process. This approach requires many degrees of freedom to uniquely map the sky, although relatively high resolution sky maps may be produced if the representation of the sky is not required to be unique. For example, the 'CLEAN' algorithm [36] commonly used in radio interferometry produces non-unique representations of the sky.

Space-based vector sensor interferometric arrays also differ from their ground-based counterparts in that each of the antenna elements is sensitive to the full sky and the array itself will generally have a fully three dimensional configuration at any instant in time. This suggests a treatment similar to that of [37] which presents an approach for scalar imaging on a sphere for non-coplanar arrays using a spherical wave harmonic transform. This approach has the significant value of allowing a spherical harmonic representation of the sky which has a natural relation to the response of the vector sensor. It also implies a sky model where estimation with a limited number of degrees of freedom implies a truncation of the spherical harmonic sequence to an appropriate degree. Extension of this work to a full polarimetric representation will be necessary to fully exploit this approach with an interferometer composed of electromagnetic vector sensors.

A spherical harmonic model of the sky seems a very natural representation for using the available degrees of freedom from a single or multiple vector sensors. Since the sky below 10 MHz has only been very coarsely mapped, a scientifically useful map of the sky could be constructed using a limited number of harmonics. Application of this approach to data from single or multiple vector sensors is ongoing and will be described in detail in a future publication.

Another similar approach is to a fit observations using a principle component based model as described in de Oliveira-Costa et. al. [38]. As with spherical harmonic fitting, this approach would enable a relatively detailed model of the sky to be constructed even with the limited degrees of freedom available from a small number of vector sensors.

7. SPACECRAFT CONCEPTUAL DESIGN

A true test of the vector sensor's capabilities requires spaceflight in order to access the sky below 10 MHz. Development of a CubeSat to demonstrate the vector sensor is underway. Elements of the CubeSat conceptual design are described here. The proposed spacecraft is a 3U design based on the MicroMAS design [39], [40]. The MicroMAS bus, including reaction wheels, orientation sensor, GPS, communications, solar panels and battery, requires approximately 1.25U. The proposed vector sensor is 1U and receivers and signal processing are another 0.25U.

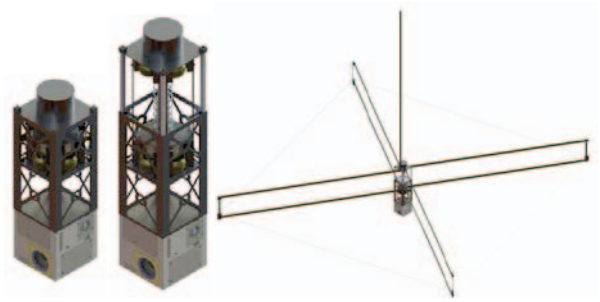

(a) (b) (c)

Figure 9. Vector Sensor CubeSat Design. The fully stowed 3U CubeSat is shown in (a), the CubeSat with the antenna section telescoped but antenna stowed in (b), and the CubeSat with the antennas completely deployed in (c). Note the thin wire horizontal loop around the deployed vertical rectangular tape spring loops in the fully deployed image. The sixth element of the vector sensor is the monopole extending upward from the CubeSat body.

Deployable Vector Sensor for CubeSats

A concept for a deployable vector antenna for CubeSat application has been developed and prototyped. The CubeSat vector antenna uses metal tape arms and wires to form two orthogonal dipoles, a monopole, and three loops. A photograph of the prototype, stowed and deployed, is shown in Figure 10. In this figure, the deployed prototype is shown in a gravity offloading test frame. This is needed so that the deploying tapes do no drag on the ground.

The CubeSat antenna prototype deploys in two stages. First, the two tape coils are separated by a telescoping boom (Figure 9 (b), Figure 10 top). The telescoping action is driven by a compressed spring. Second, the tape coils are released to unroll under their own power (Figure 9 (c), Figure 10 bottom). No motor is needed due to the strain energy within the coiled tapes. The unrolling tapes pull out the wires for the horizontal perimeter loop sections. The metal tapes themselves serve as the conductor for the four loops. The horizontal perimeter loop is fed by four wires extending back to the central hub.

The current prototype was made from off-the-shelf tape measures and 3D printed ABS plastic components. The as-built prototype with 2 m long tapes weighs approximately 1 kg. The prototype was designed for quick prototyping and testing so minimizing mass was not a concern. If the ABS components were designed to be made of aluminum with minimum mass, the total mass of the system would not grow significantly.

The antenna deployment was very repeatable for 1.5 m long tapes. When deploying with 2 m long tapes, even with the gravity offload at the tips of the loops, the gravity load along the mid-span of the tapes would sometimes cause one or more tapes to buckle before full deployment was complete. In zero gravity this buckling effect would not be an issue.

Items that still need to be addressed in the design include: considering the effects of on-orbit loads and whether they would cause buckling of the deployed tapes, ensuring proper tension in the perimeter loop wires without causing buckling of the tapes and stowing the perimeter loop wires to ensure that no snagging occurs during deployment. Several solutions to these outstanding items have been proposed and will be considered as development continues.

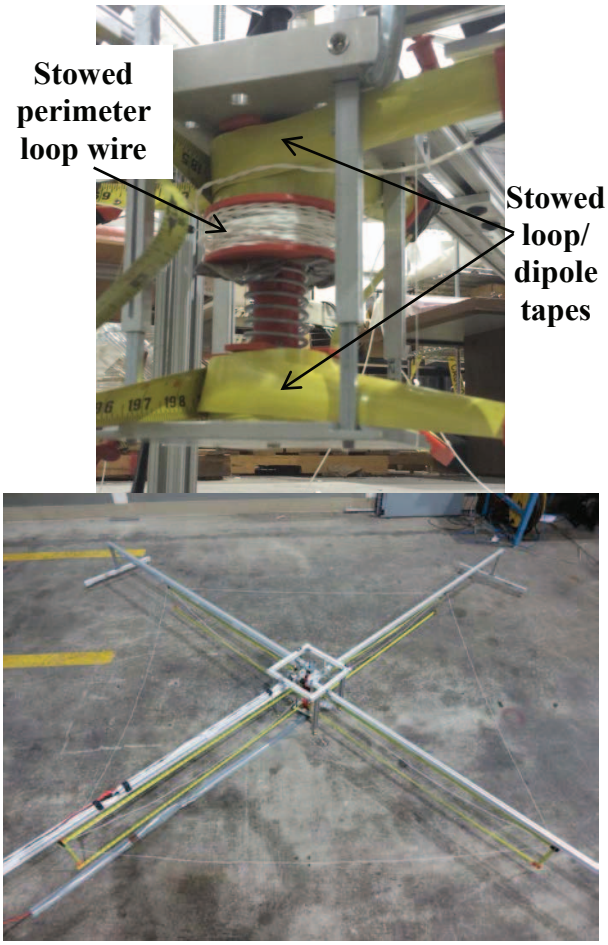

Figure 10. Stowed (top) and deployed (bottom) prototype CubeSat vector sensor. A gravity offload system was used to prevent the tape spring elements from buckling during deployment. The monopole is not shown in this image. The third loop element is composed of wire supported by the tips of the deployed tape loops/dipoles and is parallel to the ground in the above image.

A key performance metric of the vector antenna is that the measurements from each of the antenna elements are dominated by external sources rather than by internal thermal noise. This is normally accomplished by maximizing the size and the resulting effective height of the antenna subject to constraints on stowed volume, mass, and frequency independence of the element patterns. The International Telecommunications Union (ITU) provides a model of galactic noise [41] is used in the analysis below.

The ITU model predicts galactic noise, integrated over all directions, is approximately 15 dBnV/m/Hz^{½} at 5 MHz. Typical high dynamic-range radio front ends with good protection from static discharge typically provide performance of about 5 dBnV/Hz^{½} referenced to the antenna input port. To ensure that external noise dominates, an effective antenna height of at least 1 m is required (5 dBnV/Hz^{½} <<(15 dBnV/m/Hz^{½}*1m = 15 dBnV/Hz^{½}). Since the effective height of an electrically unloaded dipole is half

the physical length, a minimum antenna length of 2 m is required. This is one alternative approach to small receive system design. Often the antenna performance is analyzed based on the effective aperture [7], but for electrically small antennas it is difficult to electrically match for power transfer. By analyzing the equivalent circuit for voltage response we avoid concerns with impedance mismatch. We note that while the ITU model assumes omnidirectional sources, we are interested in determining the variation of intensity with direction.

As built, the prototype dipoles are 4 m tip-to-tip, the monopole is 2 m long, and the area of the loops are 4 m^2 for the horizontal perimeter loop and 0.8 m^2 for the two vertical loops. Increasing the size of the elements would increase their effective height but the larger loop and the dipoles are about as long as possible while providing frequency-independent element patterns. To ensure that the loop currents are equal around the loops multiple feed points are used. Two feed points are used for the smaller loops and four feed points are used for the larger loop.

On orbit calibration strategy

Receiver and array pattern calibration is critical for high resolution source location and multiple steps will be taken to ensure that the calibration is accomplished accurately.

The first is that each of the channels must be electrically balanced and the frequency response equalized so that integration of signals between elements is possible. To perform this calibration a reference signal with a well-controlled spectral content will be split and applied to each of the receiver channels just after the antenna input. The calibration signal will be under program control and will be turned off during normal data collections. A second electrical calibration will be for radiometry. A known power calibration signal will be switched into each of the receiver channels to provide a precise power reference [42]. Effective height calculation and loss analysis of the electrically small loops and dipole responses is straightforward and factors significantly into the radiometric calibration. A final calibration check is to verify the performance with external sources such as Cas A, Cyg A or Vir A as they provide both a spatially point-like source and have relatively well-known spectral intensities.

The antenna and receiver design will be verified prior to launch by testing in a near-field scanning facility similar to the SPAWAR San Diego pattern measurement range [43].

8. CONCLUSIONS AND FUTURE WORK

This study demonstrates mathematically that a single vector sensor is capable of resolving up to 19 spatially and polarimetrically separated sources. It has been shown that a vector sensor has an advantage of at least 3 dB in sensitivity over a tripole antenna. These attributes, along with the native ability to measure polarization, make the vector sensor a desirable component of an interferometric array as well as a useful stand-alone instrument. Two vector sensor prototypes, one fixed and one deployable, have been developed in order to test the above assertions about vector sensor capabilities for astronomy. These two vector sensors are currently undergoing initial testing and field testing is planned at a radio quiet site. A number of imaging algorithms have been developed and tested with simulated data.

Testing with simulated data demonstrates that a single vector sensor is capable of detecting multiple sources as well as the polarization of those sources. Algorithm refinement is still required in order to detect the 19 Gaussian sources that analysis suggests should be detectable with a single sensor. Additional algorithm work will incorporate frequency dependence to increase available degrees of freedom when mapping astronomical sources. Alternative models of the sky, such as a spherical harmonic representation, will also be considered to optimally exploit the degrees of freedom that the vector sensor offers.

The development described in this work focused primarily on the capabilities of a single vector sensor, but the longer term goal will be combining several (and eventually many) vector sensors into an interferometric array. Arraying vector sensors will provide many more degrees of freedom for imaging and will lead to much higher quality sky maps with higher effective angular resolution. It is important to note that angular resolution takes on a different meaning when using super-resolution algorithms like EM. The number of degrees of freedom available and the chosen model sets the resolution of output sky maps. This approach using vector sensors is a fundamental difference from traditional interferometric imaging where the angular resolution is set by the longest baseline of the array.

The upcoming field testing will enable future algorithm development as well as vector sensor interferometric imaging. The presence of interfering terrestrial signals will provide an opportunity to verify the nulling capabilities described in vector sensor literature [23]. Ground testing is a critical first step toward testing of a small number of vector sensors on orbit. Such an on-orbit test would be a pathfinder toward an affordable, capable space-based interferometric array for cutting edge astronomy.

ACKNOWLEDGEMENTS

The authors would like to thank the MIT-LL Advanced Concepts Committee and Line programs for their support of this effort. The spacecraft design analysis was provided by Fash Azad, and the CubeSat vector antenna mechanical design and fabrication was provided by Richard Arnold and Alec Delaney. Fabrication of the Atom antenna was accomplished by Tom Alosso and Tom Matte.

REFERENCES

[1] M. De Vos, A. W. Gunst, and R. Nijboer, "The LOFAR telescope: System architecture and signal processing," *Proc. IEEE*, vol. 97, pp. 1431–1437, 2009.

[2] S. W. Ellingson, T. E. Clarke, A. Cohen, J. Craig, N. E. Kassim, Y. Pihlstrom, L. J. Richard, and G. B. Taylor, "The Long Wavelength Array," *Proceedings of the IEEE*, 2009. [Online]. Available: http://lwa.phys.unm.edu/docs/lwa0157.pdf. [Accessed: 17-Oct-2015].

[3] G. Hallinan, "The Owens Valley LWA," in *Exascale Radio Astronomy*, 2014, vol. 2.

[4] C. J. Lonsdale, R. J. Cappallo, M. F. Morales, F. H. Briggs, L. Benkevitch, J. D. Bowman, J. D. Bunton, S. Burns, B. E. Corey, L. deSouza, S. S. Doeleman, M. Derome, A. Deshpande, M. R. Gopala, L. J. Greenhill, D. E. Herne, J. N. Hewitt, P. A. Kamini, J. C. Kasper, B. B. Kincaid, J. Kocz, E. Kowald, E. Kratzenberg, D. Kumar, M. J. Lynch, S. Madhavi, M. Matejek, D. A. Mitchell, E. Morgan, D. Oberoi, S. Ord, J. Pathikulangara, T. Prabu, A. Rogers, A. Roshi, J. E. Salah, R. J. Sault, N. U. Shankar, K. S. Srivani, J. Stevens, S. Tingay, A. Vaccarella, M. Waterson, R. B. Wayth, R. L. Webster, A. R. Whitney, A. Williams, and C. Williams, "The Murchison Widefield Array: Design Overview," *Proc. IEEE*, vol. 97, no. 8, pp. 1497–1506, Aug. 2009.

[5] C. L. Carilli and S. Rawlings, "Motivation, key science projects, standards and assumptions," *New Astron. Rev.*, vol. 48, no. 11–12, pp. 979–984, Dec. 2004.

[6] P. E. Dewdney, P. J. Hall, R. T. Schilizzi, and T. J. L. W. Lazio, "The Square Kilometre Array," *Proc. IEEE*, vol. 97, no. 8, pp. 1482–1496, Aug. 2009.

[7] S. Jester and H. Falcke, "Science with a lunar low-frequency array: From the dark ages of the Universe to nearby exoplanets," *New Astron. Rev.*, vol. 53, no. 1–2, pp. 1–26, May 2009.

[8] R. T. Groves, "Analysis of the Radio Astronomy Explorer lunar orbit mission.," in *AIAA & AAS, Astrodynamics Conference*, 1972.

[9] J. K. Alexander, M. L. Kaiser, J. C. Novaco, F. R. Grena, and R. R. Weber, "Scientific instrumentation of the Radio-Astronomy-Explorer-2 satellite," *Astron. Astrophys.*, vol. 40, pp. 365–371, 1975.

[10] J. K. Alexander and J. C. Novaco, "Survey of the galactic background radiation at 3.93 and 6.55 MHz," *Astron. J.*, vol. 79, p. 777, Jul. 1974.

[11] D. Jones, R. Allen, J. Basart, T. Bastian, B. Dennison, K. Dwarakanath, W. Ericksong, D. Finley, M. Kaiser, N. Kassim, T. Kuiperl, R. Macdowall, M. Mahoney, R. Perley, R. Preston, M. Reiner, P. O. Rodriguez, R. Stone, S. Unwin, K. O. Weiler, G. Woan, and R. Wool, "The Astronomical Low Frequency Array : Explorer Mission for Radio Astronomy A Proposed Explorer Mission for Radio Astronomy," in *Radio Astronomy at Long Wavelengths*, R. G. Stone, K. W. Weiler, M. L. Goldstein, and J.-L. Bougeret, Eds. American Geophysical Union, 2000, pp. 339–349.

[12] R. J. MacDowall, S. D. Bale, L. Demaio, N. Gopalswamy, D. L. Jones, M. L. Kaiser, J. C. Kasper, M. J. Reiner, and K. W. Weiler, "Solar Imaging Radio Array (SIRA): A multi-spacecraft mission," in *Enabling Sensor and Platform Technologies for Spaceborne Remote Sensing*, vol. 5659, no. May 2012, G. J. Komar, J. Wang, and T. Kimura, Eds. 2005, pp. 284–292.

[13] J. O. Burns, J. Lazio, S. Bale, J. Bowman, R. Bradley, C. Carilli, S. Furlanetto, G. Harker, A. Loeb, and J. Pritchard, "Probing the first stars and black holes in the early Universe with the Dark Ages Radio Explorer (DARE)," *Adv. Sp. Res.*, vol. 49, no. 3, pp. 433–450, Feb. 2012.

[14] M. Bentum and A. J. Boonstra, "OLFAR - Orbiting Low Frequency Antenna for Radio Astronomy," *20th Annu. Work. Circuits, Syst. Signal Process. ProRISC*, pp. 1–6, 2009.

[15] M. E. Knapp, "SOLARA/SARA: first steps toward a space-based radio interferometry constellation," in *65th International Astronautical Congress (IAC)*, 2014.

[16] D. Oberoi and J.-L. Pinçon, "A new design for a very low frequency space borne radio interferometer," in *American Geophysical Union Fall Meeting*, 2003, no. 1988, p. 17.

[17] K. T. Wong and M. D. Zoltowski, "Uni-Vector-Sensor ESPRIT for Multisource Azimuth, Elevation, and Polarization Estimation," *IEEE Trans. Antennas Propag.*, vol. 45, no. 10, pp. 1467–1474, 1997.

[18] F. C. Robey, "High Frequency Geolocation and System Characterization (HFGeo) Phase 1B Proposers' Day Briefing: HFGeo Phase 0 and Phase 1B Test and Evaluation," 2012. [Online]. Available: http://www.iarpa.gov/images/files/programs/hfgeo/120710_Phase1B_Proposers_Day_Part2.pdf.

[19] K. T. Wong and M. D. Zoltowski, "Closed-form direction finding and polarization estimation with arbitrarily spaced electromagnetic vector-sensors at unknown locations," *IEEE Trans. Antennas Propag.*, vol. 48, no. 5, pp. 671–681, 2000.

[20] A. Nehorai and E. Paldi, "Vector-sensor array

processing for electromagnetic source localization," *IEEE Trans. Signal Process.*, vol. 42, no. 2, pp. 376–398, 1994.

[21] A. Nehorai, K. C. Ho, and B. T. G. Tan, "Minimum-noise-variance beamformer with an electromagnetic vector sensor," *IEEE Trans. Signal Process.*, vol. 47, no. 3, pp. 601–618, 1999.

[22] K. Han and A. Nehorai, "Nested vector-sensor array processing via tensor modeling," *IEEE Trans. Signal Process.*, vol. 62, no. 10, pp. 2542–2553, 2014.

[23] P. Pal and P. P. Vaidyanathan, "Nested arrays: A novel approach to array processing with enhanced degrees of freedom," *IEEE Trans. Signal Process.*, vol. 58, no. 8, pp. 4167–4181, 2010.

[24] F. C. Robey, "A Covariance Modeling Approach to Adaptive Beanmforming and Detection," *MIT Lincoln Lab. Tech. Rep. 918*, 1991.

[25] T. K. Moon, "The expectation-maximization algorithm," *IEEE Signal Process. Mag.*, vol. 13, no. 6, pp. 47–60, 1996.

[26] A. P. Dempster, N. M. Laird, and D. B. Rubin, "Maximum Likelihood from Incomplete Data via the EM Algorithm," *J. R. Stat. Soc. Ser. B*, vol. 39, no. 1, pp. 1–38, 1977.

[27] J. A. Fessler and A. O. Hero, "Space-alternating generalized expectation-maximization algorithm," *IEEE Trans. Signal Process.*, vol. 42, no. 10, pp. 2664–2677, 1994.

[28] N. Parikh and S. Boyd, "Proximal algorithms," *Found. Trends Optim.*, vol. 1, no. 3, pp. 123–231, 2013.

[29] P. J. Chung and J. F. Böhme, "DOA estimation using fast EM and SAGE algorithms," *Signal Processing*, vol. 82, no. 11, pp. 1753–1762, Nov. 2002.

[30] S. Boyd and L. Vandenberghe, *Convex Optimization*. Cambridge, U.K.: Cambridge University Press, 2004.

[31] K. Scheinberg, D. Goldfarb, and X. Bai, "Fast First-Order Methods for Composite Convex Optimization with Backtracking," *Found. Comput. Math.*, vol. 14, no. 3, pp. 389–417, Mar. 2014.

[32] B. O'Donoghue and E. Candès, "Adaptive Restart for Accelerated Gradient Schemes," *Found. Comput. Math.*, vol. 15, no. 3, pp. 715–732, Jul. 2013.

[33] K. M. Gorski, E. Hivon, A. J. Banday, B. D. Wandelt, F. K. Hansen, M. Reinecke, and M. Bartelmann, "HEALPix: A Framework for High-Resolution Discretization and Fast Analysis of Data Distributed on the Sphere," *Astrophys. J.*, vol. 622, no. 2, pp. 759–771, Apr. 2005.

[34] J. T. Kent, "The Fisher-Bingham Distribution on the Sphere," *J. R. Stat. Soc. Ser. B*, vol. 44, no. 1, pp. 71–80, 1982.

[35] NIST, "Radio Station WWV," 2015. [Online]. Available: http://www.nist.gov/pml/div688/grp40/wwv.cfm.

[36] J. A. Högbom, "Aperture Synthesis with a Non-Regular Distribution of Interferometer Baselines," *Astron. Astrophys. Suppl.*, vol. 15, 1974.

[37] T. D. Carozzi, "Imaging on a sphere with interferometers: the spherical wave harmonic transform," *Mon. Not. R. Astron. Soc. Lett.*, vol. 451, no. 1, pp. L6–L10, May 2015.

[38] A. A. de Oliveira-Costa, M. Tegmark, B. M. Gaensler, J. Jonas, T. L. Landecker, and P. Reich, "A model of diffuse Galactic radio emission from 10 MHz to 100 GHz," *Mon. Not. R. Astron. Soc.*, vol. 388, no. 1, pp. 247–260, Jul. 2008.

[39] K. Cahoy, W. J. Blackwell, G. Allen, M. Bury, R. Efromson, C. Galbraith, T. Hancock, V. Leslie, I. Osaretin, L. Retherford, M. Scarito, M. Shields, D. Toher, K. Wight, D. Miller, A. Marinan, S. Paek, E. Peters, F. H. Schmidt, B. Alvisio, E. Wise, R. Masterson, D. Franzim Miranda, C. Crail, R. Kingsbury, A. Souffrant, L. Orrego, G. Eslinger, A. Nicholas, and C. Pong, "The MicroMAS CubeSat Mission," *AGU Fall Meet. Abstr.*, vol. -1, p. 2162, Dec. 2012.

[40] W. Blackwell, G. Allen, C. Galbraith, R. Leslie, I. Osaretin, M. Scarito, M. Shields, E. Thompson, D. Toher, D. Townzen, A. Vogel, R. Wezalis, K. Cahoy, D. Miller, A. Marinan, R. Kingsbury, E. Wise, S. W. Paek, E. Peters, M. Prinkey, P. Davé, B. Coffee, and N. Erickson, "MicroMAS: A First Step Towards a Nanosatellite Constellation for Global Storm Observation," *AIAA/USU Conference on Small Satellites*. 2013.

[41] International Telecommunication Union, *Radio noise P Series Radiowave propagation*, vol. 11. 2013.

[42] R. H. Dicke, "The Measurement of Thermal Radiation at Microwave Frequencies," *Rev. Sci. Instrum.*, vol. 17, no. 7, p. 268, 1946.

[43] SPAWAR Systems Center PACIFIC, "Antenna Pattern Range." [Online]. Available: http://www.public.navy.mil/spawar/pacific/cis/documents/antenna pattern range.pdf.

BIOGRAPHY

Mary Knapp *received a BS in Aerospace Engineering at MIT in 2011 and is currently a 4th year graduate student in MIT's Department of Earth, Atmospheric, and Planetary Science. She was awarded and NSF Graduate Research Fellowship in 2012. Her research focus is the detection and characterization of exoplanetary magnetic fields via low frequency radio emission. Her additional research interests include the development of small spacecraft for astronomy and planetary science She has participated in the development of the CubeSat ExoplanetSat (now renamed ASTERIA) since 2010. ExoplanetSat was developed at MIT for several years and is now in final development at JPL with an expected launch in late 2016/early 2017.*

Dr. Frank Robey *received BSEE (Summa Cum Laude) and MSEE degrees from U. Missouri-Columbia and D.Sc. EE in adaptive detection and beamforming from Washington U. He has been with MIT Lincoln Laboratory for 25 years. At Lincoln he has been the lead for multiple fundamental and applied research initiatives including advanced sensor technology, coherent Multiple-Input Multiple-Output (MIMO) radar, electronic intelligence and next generation over-the-horizon radar. He spent two years on assignment as the Deputy Director of Smart Collection at IARPA/ODNI. He began his career as a precision instrument designer at Hewlett Packard and then at Emerson Electric.*

Dr. Ryan Volz *received a BS degree in Aerospace Engineering from the Pennsylvania State University in 2007, an M.Phil degree in Engineering (Control Systems) from the University of Cambridge in 2008, and MS and PhD degrees in Aeronautics and Astronautics from Stanford University in 2009 and 2015, respectively. He was awarded an NDSEG graduate fellowship in 2008 and received third prize at the international URSI GASS 2011 student paper competition. He is currently a postdoctoral associate at the MIT Haystack Observatory researching radio measurement and signal processing methods that leverage sparsity.*

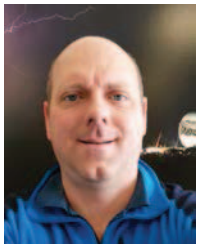

Dr. Frank D. Lind *studied at the University of Washington where he received a BS degree in Physics (with honors) and a BS degree in Computer Science in 1994. He then joined the UW Geophysics Program and pursued studies leading to the Doctor of Philosophy in Geophysics in 1999. His work there focused on Passive Radar Observations of the Aurora Borealis. He has worked at MIT Haystack Observatory for 15 years. His scientific and technical research focuses on radar and radio studies of the space environment, passive radar, incoherent scatter radar, ionospheric plasma physics, software radio and radar signal processing, and distributed sensor systems. At the Observatory he leads the technical team for the NSF sponsored Millstone Hill Geospace Facility and instrument development efforts for a variety of advanced radio telescopes, array radars, and distributed sensor networks. He is the former chair of USNC URSI Commission G.*

Dr. Alan J. Fenn *received a BS degree from the University of Illinois–Chicago and MS and PhD degrees from The Ohio State University, all in electrical engineering. He is a senior staff member in the RF Technology Group in the Advanced Technology Division at MIT Lincoln Laboratory. He is currently involved in the development of novel ultrawideband antennas and phased arrays for radar and communications applications. In 2000, Dr. Fenn was elected a Fellow of the IEEE for his contributions to the theory and practice of adaptive phased-array antennas. He is an author of more than 70 journal articles and conference papers in the field of antennas and adaptive phased array systems. He received the IEEE Antennas and Propagation Society's 1990 H.A. Wheeler Applications Prize Paper Award and the IEEE/URSI-sponsored 1994 International Symposium on Antennas JINA Award. He is currently serving as technical program chair for the 2016 IEEE International*

Symposium on Phased Array Systems and Technology.

Alex Morris *received the B.S. and M.S. degrees in electrical engineering from the University of Alaska Fairbanks, in 2011 and 2014, respectively. Since then, he has been with M.I.T. Lincoln Laboratory in Lexington, MA, where holds the position of associate technical staff.*

Dr. Mark J. Silver *received a BS degree from the University of Wisconsin–Madison in engineering mechanics and MS and PhD degrees from the University of Colorado–Boulder in aerospace engineering. He is a staff member in the Mechanical Engineering Group in the Engineering Division at MIT Lincoln Laboratory. He has been with MIT Lincoln Laboratory for 5 years working in the area of design and analysis of terrestrial and spacecraft structures. His research areas include deployable spacecraft structures, precision alignment, composite materials and emerging computational analysis tools.*

Dr. Sarah Klein *received BS and MS degrees in Physics from Georgia Tech and Ph.D. in Physics from U. South Florida. She has been with MIT Lincoln Laboratory for 19 years. She has led numerous programs in both fundamental research and development of novel optical sensor systems successfully deployed in space, air, and ground platforms. Her research in optical remote sensing includes lidar, Earth and atmospheric monitoring, space situational awareness, and free space laser communication. She spent three years on assignment with the USAF Space and Missile Systems Center as government lead developing next generation optical and RF satellite communication systems.*

Professor Sara Seager *is an astrophysicist and planetary scientist at MIT. Her science research focuses on theory, computation, and data analysis of exoplanets. Her research has introduced many new ideas to the field of exoplanet characterization, including work that led to the first detection of an exoplanet atmosphere. Professor Seager also works in space instrumentation and space missions for exoplanets, including CubeSats, as a co-I on the MIT-led TESS, a NASA Explorer Mission to be launched in 2017, and chaired the NASA Science and Technology Definition Team for a "Probe-class" Starshade and telescope system for space-based direct imaging discovery and characterization of Earth analogs. Among other awards, Professor Seager is the 2012 recipient of the Raymond and Beverly Sackler Prize in the Physical Sciences, a 2013 MacArthur Fellow, and was elected to the National Academy of Sciences in 2015.*